Artificial ionospheric modification

Caton, Ronald; Pederson, Todd; Groves, Keith; Hines, Jack; Cannon, Paul S.; Jackson-Booth, Natasha; Parris, Richard T.; Holmes, Jeffrey M.; Su, Yi-Jiun; Mishin, Evgeny V.; Roddy, Patrick A.; Viggiano, Albert A.; Shuman, Nicholas S.; Ard, Shaun G.; Bernhardt, Paul A.; Siefring, Carl L.; Retterer, John; Kudeki, Erhan; Reyes, Pablo M.

DOI:
10.1002/2016RS005988

AGU PUBLICATIONS

Radio Science

RESEARCH ARTICLE
10.1002/2016RS005988

Special Section:
2013 Equatorial Ionospheric Sounding Rocket Campaign from Kwajalein Atoll

Artificial ionospheric modification: The Metal Oxide Space Cloud experiment

Ronald G. Caton[1], Todd R. Pedersen[1], Keith M. Groves[2], Jack Hines[1,3], Paul S. Cannon[4,5], Natasha Jackson-Booth[4], Richard T. Parris[1], Jeffrey M. Holmes[1], Yi-Jiun Su[1], Evgeny V. Mishin[1], Patrick A. Roddy[1], Albert A. Viggiano[1], Nicholas S. Shuman[1], Shaun G. Ard[2], Paul A. Bernhardt[6], Carl L. Siefring[6], John Retterer[2], Erhan Kudeki[7], and Pablo M. Reyes[7]

[1]Space Vehicles Directorate, Air Force Research Laboratory, Kirtland Air Force Base, Albuquerque, New Mexico, USA, [2]Institute for Scientific Research, Boston College, Chestnut Hill, Massachusetts, USA, [3]Now at Space Dynamics Laboratory, Logan, Utah, USA, [4]QinetiQ, Malvern, United Kingdom, [5]Now at University of Birmingham, Birmingham, United Kingdom, [6]Plasma Physics Division, Naval Research Laboratory, Washington, District of Columbia, USA, [7]Department of Electrical and Computer Engineering, University of Illinois at Urbana-Champaign, Urbana, Illinois, USA

Key Points:
- An overview of the 2013 Metal Oxide Space Cloud (MOSC) sounding rocket experiment from Kwajalein Atoll
- A comprehensive diagnosis of artificial plasma clouds generated through release of samarium vapor in the upper atmosphere
- Artificial modification of the radio frequency propagation environment

Correspondence to:
R. G. Caton,
Ronald.Caton.1@us.af.mil

Citation:
Caton, R. G., et al. (2017), Artificial ionospheric modification: The Metal Oxide Space Cloud experiment, *Radio Sci.*, *52*, doi:10.1002/2016RS005988.

Received 24 FEB 2016
Accepted 7 SEP 2016

Abstract Clouds of vaporized samarium (Sm) were released during sounding rocket flights from the Reagan Test Site, Kwajalein Atoll in May 2013 as part of the Metal Oxide Space Cloud (MOSC) experiment. A network of ground-based sensors observed the resulting clouds from five locations in the Republic of the Marshall Islands. Of primary interest was an examination of the extent to which a tailored radio frequency (RF) propagation environment could be generated through artificial ionospheric modification. The MOSC experiment consisted of launches near dusk on two separate evenings each releasing ~6 kg of Sm vapor at altitudes near 170 km and 180 km. Localized plasma clouds were generated through a combination of photoionization and chemi-ionization ($Sm + O \rightarrow SmO^+ + e^-$) processes producing signatures visible in optical sensors, incoherent scatter radar, and in high-frequency (HF) diagnostics. Here we present an overview of the experiment payloads, document the flight characteristics, and describe the experimental measurements conducted throughout the 2 week launch window. Multi-instrument analysis including incoherent scatter observations, HF soundings, RF beacon measurements, and optical data provided the opportunity for a comprehensive characterization of the physical, spectral, and plasma density composition of the artificial plasma clouds as a function of space and time. A series of companion papers submitted along with this experimental overview provide more detail on the individual elements for interested readers.

1. Introduction

As early as the 1950s, experiments involving ionospheric modification for the purpose of tailoring the radio propagation environment were conducted from sounding rocket platforms. In a review paper of ionospheric chemical releases, *Davis* [1979] discusses work by *Edwards et al.* [1955] resulting in the first ever upper atmospheric chemical release from a sounding rocket. Their experiment involved the release of sodium vapor from multiple canisters, each containing 1 kg of sodium pellets mixed with finely powdered iron oxide and aluminum. In the following decades, a number of chemical release experiments were performed using both suborbital rockets and orbital platforms. Dozens of successful experiments have probed the characteristics of vaporized barium (Ba), for example, the Combined Release and Radiation Effects Satellite Experiment (CRRES) [*Huba et al.*, 1992; *Bernhardt*, 1992; *Giles et al.*, 1995; *Hunton et al.*, 1998], the Cameo (Chemically Active Material Ejected in Orbit) experiment [*Heppner et al.*, 1981], and numerous sounding rocket missions [e.g., *Kelley et al.*, 1974; *Rosenberg and Best*, 1971]. From 1961 to 1972, researchers from the Max Planck Institute for Extraterrestrial Physics conducted a total of 66 sounding rocket launches with Ba canister payloads [*Lüst*, 2001]. Both neutral and ionized components of the resulting Ba clouds were tracked providing measurements of high altitude winds and electric fields as well as comprehensive diagnostics of the reaction rates between Ba and the background atmospheric constituents. *Zabusky et al.* [1973] reported ion densities on the order of 10^7 cm^{-3} from Ba releases in twilight during the 1971 Spruce experiment. More closely related to the goals of the MOSC experiment, other researchers have examined the effect of artificially modified ionospheres on HF propagation. During the Negative Ion Cation Release Experiment 2 (NICARE 2), HF propagation channel characteristics on a single link from two sites in the Republic of the Marshall

Islands were studied under the influence of large electron density depletions created by the release of sulfur hexafluoride (SF6) [*Fitzgerald et al*., 1997]. And in the Coloured Bubbles Experiment, Ba packages were detonated in the upper atmosphere and aircraft measurements of UHF Satellite Communication (SATCOM) links analyzed to show direct impact of the recorded phase and amplitude measurements in the shadow of the result cloud [*Johnson and Hocutt*, 1984; *Çakir et al*., 1992]. Barium clouds released in sunlight quickly produce atomic ions that will not recombine for days. The CRRES G-12 Barium Release from Puerto Rico at dusk in sunlight was detected the next morning by a Russian ship with cameras viewing the barium ion cloud glow [*Milinevsky et al*., 1993].

In an examination of materials with exothermic chemi-ionization reactions providing the potential for long-lived artificially generated plasma clouds, researchers at the U.S. Air Force Research Laboratory (AFRL) turned their attention to the lanthanide series of metals. *Murad and Hildenbrand* [1980] reported on the disassociation energies of the lanthanide monoxide series, and *Murad* [1984] further expanded on this study analyzing the anticipated reaction between Sm^+ with O_2. Results from these studies and subsequent testing by *Files et al.* [2007] led to the development of canister payloads packed with a titanium/boron mixture (TiB) and powdered samarium (Sm) consisting of a ~30% mixture of Sm by volume. While other metals were considered, Sm was chosen due to the achievable vaporization temperature when mixed with an intermetallic heat source. Sm canisters had flown on at least two previous experiments [*Larsen et al*., 1989; *Stokes and Murphy*, 1987]; however, no direct measurements were made of the resulting plasma densities.

The MOSC experiment was designed to provide an opportunity for the first comprehensive diagnosis of an artificially plasma cloud generated by the release of Sm vapor in the upper atmosphere. Of primary interest was an examination of the extent to which a tailored radio frequency (RF) propagation environment could be generated through artificial ionospheric modification. This included an investigation into the potential use of this technology for suppression of scintillation caused by ionospheric irregularities driven by the Rayleigh-Taylor instability (RTI) in the nighttime equatorial region [*Kelley et al*., 2011; *Makela et al*., 2006]. Amongst other requirements, site selection called for a low-latitude release close to an incoherent scatter radar facility capable of tracking the resulting plasma clouds.

2. Experiment Description

During the 2013 MOSC experiment high-density ionization clouds created through the release of Sm metal vapor in the upper atmosphere were probed to fully characterize its position, velocity, and density as a function of time. Sounding rockets carrying the MOSC payload were launched near dusk on 1 and 9 May 2013 from the Reagan Test Site on Kwajalein Atoll, home to the Advanced Research Project Agency (ARPA) Long-Range Tracking and Instrumentation Radar (ALTAIR) used to track the resulting plasma clouds providing the requisite incoherent scatter diagnostics. Prior to launch, sensors were installed on five islands across four atolls: Kwajalein Island and Roi-Namur Island (Kwajalein Atoll), Wotho Atoll, Rongelap Atoll, and Likiep Atoll (Figure 1). A complete description of the ground instrumentation follows in section 2.2.

2.1. Flight Payload

The scientific payload for each MOSC flight consisted of two canisters and a dual-band Coherent Electromagnetic Radio Tomography (CERTO) beacon transmitter [*Bernhardt and Siefring*, 2006]. The cylindrical canisters were packed with an intermetallic mix (titanium-boron, TiB) and powdered Sm and stacked back to back in a single deck with exhaust port holes aligned 180° apart. Each canister contained a ~30% mixture of Sm by volume (~7.8 kg of TiB, ~3.30 kg of Sm) with a total filled mass of ~21.25 kg. The Sm canisters were ignited in flight with programmed timer squibs. Vaporized Sm was vented through ~3.5 MPa (500 psi) burst disks. Thermistors were installed on each canister providing temperature readouts from upper and lower portions of the canisters as well as near the burst disk. Dual-band CERTO beacon instruments were included on each MOSC flight vehicle providing an opportunity for direct probing of the plasma cloud with VHF (~150 MHz) and UHF (~400 MHz) transmissions. Evaluation of the phase differences recorded on any of nine ground receivers fielded during the experiment provided line-of-sight estimates of the total electron content (TEC).

2.2. Ground Hardware Systems

With only ~70 square miles of land mass spanning a sea area of more than 750,000 square miles, the Republic of the Marshall Islands offers limited sites for the installation of scientific instrumentation. Critical diagnostics

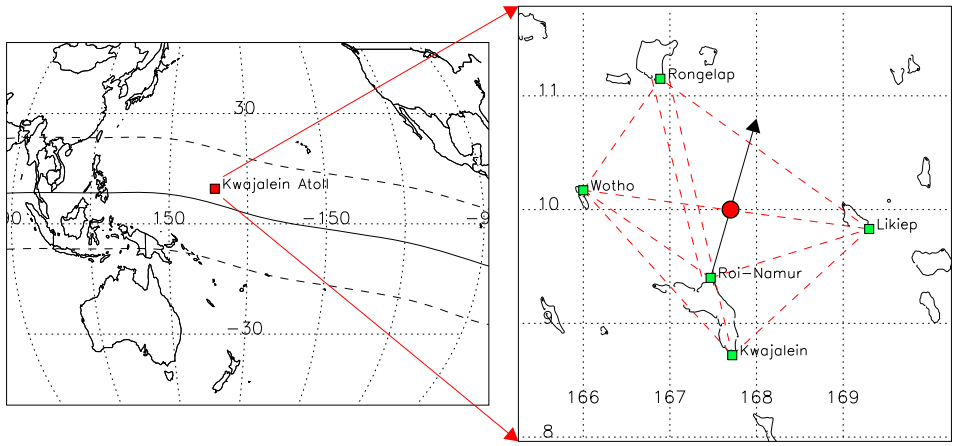

Figure 1. Site diagram for diagnostic sites deployed for the 2013 MOSC Sounding Rocket Experiment: Wotho, Rongelap, Likiep, Roi-Namur, and Kwajalein. The black arrow represents the flight path, and the approximate location of the samarium vapor release is highlighted with a red circle. Red dashed lines indicate nominal HF propagation paths between transmitters and receivers.

for each launch were provided by incoherent scatter observations with the ALTAIR radar providing direct measurements of the plasma density within the MOSC clouds. With its fully steerable 46 m dish with dual frequency (VHF/UHF) capabilities and >6 MW peak power, ALTAIR has provided valuable data for a number of ionospheric research experiments [e.g., *Tsunoda et al*., 1979; *Knepp and Houpis*, 1991; *Mendillo et al*., 1992; *Tsunoda*, 1995; *Hysell et al*., 2005; *Kudeki et al*., 2006; *Cannon et al*., 2006; *Caton et al*., 2009]. An overview of the additional MOSC sensors and their significance to the overall experiment is provided in Table 1. A comprehensive list of instruments by site can be found in the Appendix A.

To best quantify the impact of the MOSC plasma cloud on the high-frequency (HF) propagation environment, swept sounding with a continuous chip waveform and fixed-frequency pulse compressed (delay Doppler) transmissions [*Jackson-Booth et al*., 2012] was employed with transmitter-receiver paths up to 300+ km configured in the north-south and east-west directions (as shown in Figure 1). A complete description of the locations and types HF of transmitters and receivers used during MOSC can be found in the Appendix A. Both MOSC releases occurred near the direct path between the Likiep and Wotho Atolls.

2.3. MOSC Flight Characteristics

Lift-off of the first of two MOSC launches (MOSC-1) occurred at 07:38:00 UT on 1 May 2013. The second launch (MOSC-2) followed on 9 May 2013 at 07:23:00 UT. Nightly launch window timing considerations included the location of the solar terminator relative to the anticipated release location in order to provide several minutes of solar illumination of the cloud. The nominal flight plan for MOSC-1 called for the release of Sm vapor at an altitude of 190 km on the upleg with the apogee at 212 km. A squib ignition timer, programed for 159.9 s into the flight, triggered the intermetallic heat source and subsequent chemical release. Postlaunch analysis indicated an underperformance of the Terrier MK70-Improved Orion reaching an apogee of only 185 km with the MOSC release occurring at 170.5 km.

Table 1. Diagnostic Instruments for the MOSC Experiment

Instrument	Sensor/Signal	Derived Measurement
Coherent backscatter radar	Backscatter EM phase/amplitude	Small-scale irregularities and irregularity drift
Ground optics	Integrated volume emission from photons; spectral observations	Integrated neutral and ion density/cloud shape-dimensions-spectral composition
Radio beacon	Radio phase/amplitude	Scintillation and absolute TEC
Incoherent scatter radar	Backscatter EM phase/amplitude	Electron density profile and temperature
HF multichannel probe/ionosonde	Reflected EM phase/amplitude	Bottomside structure, plasma density profiles, and peak plasma densities
Scintillation Network Decision Aid (SCINDA) ground receivers	Radio phase/amplitude at UHF and GPS	Scintillation and absolute TEC

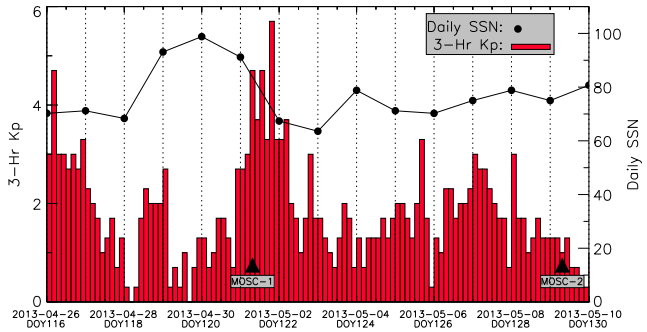

Figure 2. A 3 h *Kp* (red) and daily sunspot number (SSN, black) during the MOSC launch window. Triangles denote time periods for the two MOSC launches.

MOSC-1 was launched into the most geomagnetically active conditions experienced within the 2 week experiment window. At launch (07:38 UT), the 3 h Planetary *K* index (*Kp*) was 4+ reaching 5+ later in the evening as seen in Figure 2. While the elevated *Kp* levels and subsequent substorm activity were not optimal conditions, launch consideration was constrained by the nightly presence of strong tropical winds, limited opportunities for optical observations, and range sharing with another mission. On this evening, spread *F* activity was observed at an unusually early hour with significant scintillation measured on a link to an overhead geosynchronous satellite just after 08:00 UT (20:00 MHT, Marshall Islands Standard Time and 19:20 LT, solar local time). The activity continued until nearly 14:00 UT and was followed by extremely rare scintillation activity during sunlight hours from 19:30 to 21:30 UT (07:30–09:30 MHT) as seen in Figure 13. Data from Defense Meteorology Satellite Program (DMSP) satellites on the evening of 1 May 2013 indicate the presence of storm time penetration electric fields coincident with the MOSC-1 launch which were observed to have a dramatic effect on the cloud morphology (see section 3).

The squib timer for the MOSC-2 launch was programmed for a nominal release at 200 km ($T + 177.5$ s), slightly below the expected apogee of 212 km. As with the first launch, underperformance of the rocket resulted in a release at 182 km, 18 km below the intended target. The earlier launch time (07:23 UT) provided an extended period of observation with ground-based optical sensors. The MOSC-2 launch occurred under what would be considered a typical evening during the spring season in the northern Pacific sector. *Kp* varied between 1− and 1+ throughout the evening with a daily sunspot value of 76. Within 2 h after sunset, fully developed ionospheric plumes were observed to the west drifting toward the location of the MOSC-2 release.

3. Data Summary and Discussion

In this section, we present initial results and discuss representative data types from sensors used to diagnose the MOSC plasma clouds. More detailed analysis of data collected and models developed from the experiment will be submitted as companion articles.

3.1. Telemetry

Radar tracking and telemetry streams from onboard sensors were made available for postflight analysis. Data reduction of positional information including elapsed time, altitude, range, horizontal range, velocity, latitude, longitude, *X*, *Y*, *Z*, and GMT time were provided at 10 Hz with an accuracy of 0.1 s and/or 50 m of position based on radar tracking of onboard transponders from Kwajalein Island. A GPS receiver system included in the payload electrical section of each MOSC vehicle tracked the GPS L1 (1575.42 GPS) carrier at 20 Hz.

3.2. Incoherent Scatter Radar

The ALTAIR radar provided direct measurements of the plasma density within the MOSC clouds and operated nightly throughout the experiment window providing background ionospheric recordings. A series of fixed-point, meridional, and zonal scans were performed each evening beginning approximately 1 h before to the opening of the nightly launch window. Just prior to launch, the dish was positioned into fixed-point staring mode aimed at the nominal release location. Updated coordinates were provided approximately 30 s after burnout allowing for capture of the release within the 1° UHF (422 MHz) and 3° VHF (158 MHz) beams. Seconds after release, a narrow raster scanning mode was initiated centered on operator defined coordinates guided by MOSC cloud position updates from optical sensors. After ~10 min, a wider raster scan was used to track the cloud motion before transitioning to a series of meridional and zonal scans continuing to monitor both the cloud and the ionospheric background.

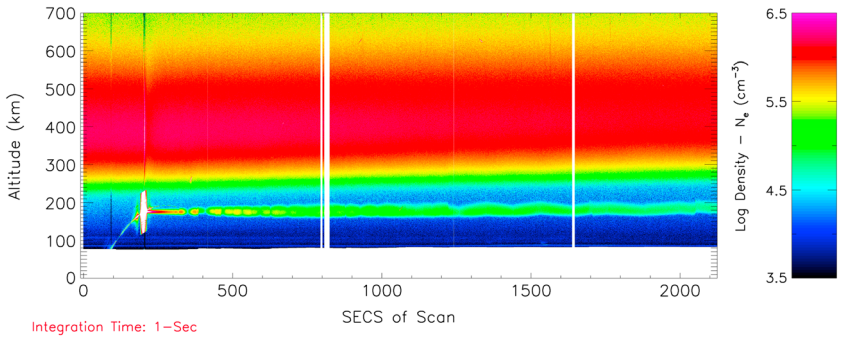

Figure 3. ALTAIR returns on UHF during the MOSC-2 flight.

In Figure 3, we present UHF returns at ALTAIR recorded during the first ~30 min of the MOSC-2 flight. The MOSC-2 rocket appears in the radar side lobe at ~100 s into the scan with initiation of the Sm canister at ~200 s. In Figure 4, incoherent scatter from the MOSC cloud is visible near 200 km in a zonal scan beginning at ~ T + 43 min, or ~40 min after the Sm vapor release. Direct evidence of the MOSC plasma cloud was seen in ALTAIR for ~2.5 h.

Integrating ALTAIR returns and building a time series of density profiles during the first ~20–30 min during optical observation of the cloud provides temporal and spatial diagnostics of the early cloud development. For example, a 5 s integrated profile generated ~1 min after the MOSC-2 release on 9 May 2013 showed evidence of an artificially created layer with log densities up to 6.33 cm^{-3}, equivalent to a plasma frequency of ~13.13 MHz. With further processing of the cloud density profiles, we are able to obtain estimates of the integrated TEC within the cloud along the look direction of the radar. Pairing these observations with ground-based optics provided the necessary diagnostics for development of the MOSC Cloud Model discussed later in this paper.

In addition to the fixed-point and raster scanning techniques used specifically for characterization of the MOSC clouds, ALTAIR was operated in routine sequential scan modes where the beam was pointed first perpendicular to the local magnetic field (field aligned or FA) and then just off of perpendicularity (off perp or OP). In FA mode, coherent Bragg backscatter is returned from irregularities at one half the radar wavelength [*Towle*, 1980; *Hysell et al*., 1994]. When the beam is pointed OP, true density measurements are available often highlighting the presence of *F* region density depletions or plumes. Sequential FA (top) and OP (bottom) scans are displayed in Figure 5 from the evening of the MOSC-2 launch on 9 May 2013. In Figure 5 (top), UHF returns from an ALTAIR FA scan are displayed for an ~8 min east-to-west scan. The beam is pointed perpendicular to the magnetic field at ~300 km, and the radar is sensitive to coherent backscatter from turbulence on the scale of ~0.35 m, half the radar UHF (422 MHz) wavelength. Density measurements are not possible in regions of backscatter, so the regions are colored white mapping the extent of the turbulent regions. For the subsequent radar scan, the antenna was tilted ~6° to the north and is now OP. As seen in Figure 5 (bottom), the OP scan, begun ~97 s after completion of the FA scan allowing time for repositioning of the dish, density measurements provide evidence of ionospheric plumes along with a highly structured bottomside.

3.3. Optical Data

Optical sensors were deployed on both Kwajalein and Rongelap Atolls for diagnosis of the MOSC plasma clouds. In addition to narrow-field cameras which recorded the cloud movement and development, both locations were equipped with all-sky imagers and optical spectrometers for measurements of the cloud's chemical signature. Data from the optical sensors were used in real time to guide raster scan observations from ALTAIR and were considered critical for GO/NO-GO decisions on launch nights. In Figure 6, we see an image recorded from Roi-Namur during MOSC-1 on a Nikon D90 with a 50 mm F/1.2 Nikkor lens, 3 s exposure, and an ISO of 3200. It is a true color raw image with a white balance of 4000 K showing the distinct separation of the red and blue components of the clouds observed during both releases.

While ALTAIR provided high-resolution density probing of the cloud, it is only though the merging of the radar scans with data from local all-sky imagers that we can know precisely which portion of the cloud we

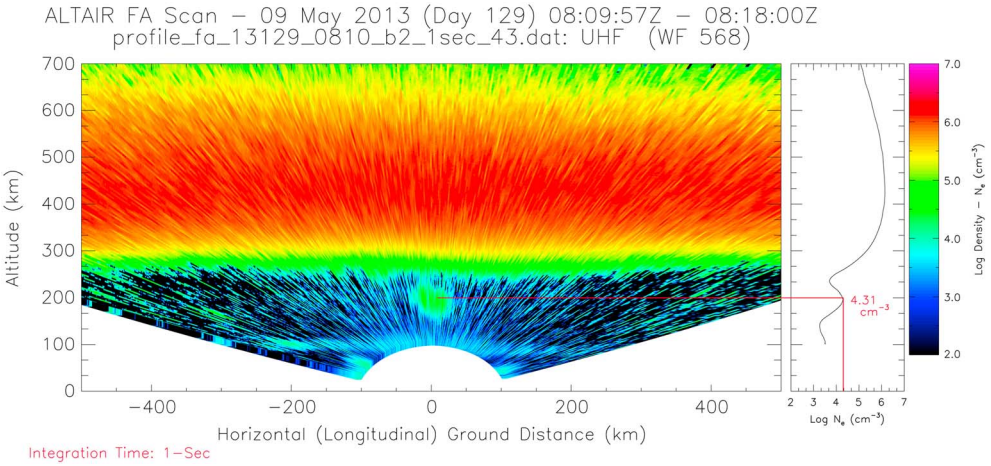

Figure 4. Spatial view of the MOSC-2 cloud from an ALTAIR zonal scan beginning at ~ T + 43 min.

were scanning with the radar. Intensities on the all-sky images were used to map the full spatial density structure of the optical cloud. Optical data from an all-sky camera near the launch site on Roi-Namur provided 180° degree field-of-view images at six different wavelengths (unfiltered, 4278 Å, 5577 Å, 6300 Å, 7774 Å, and 8446 Å) each minute. An example of how the optical and radar data were combined in the development of a cloud model is provided in section 4.1 of this report.

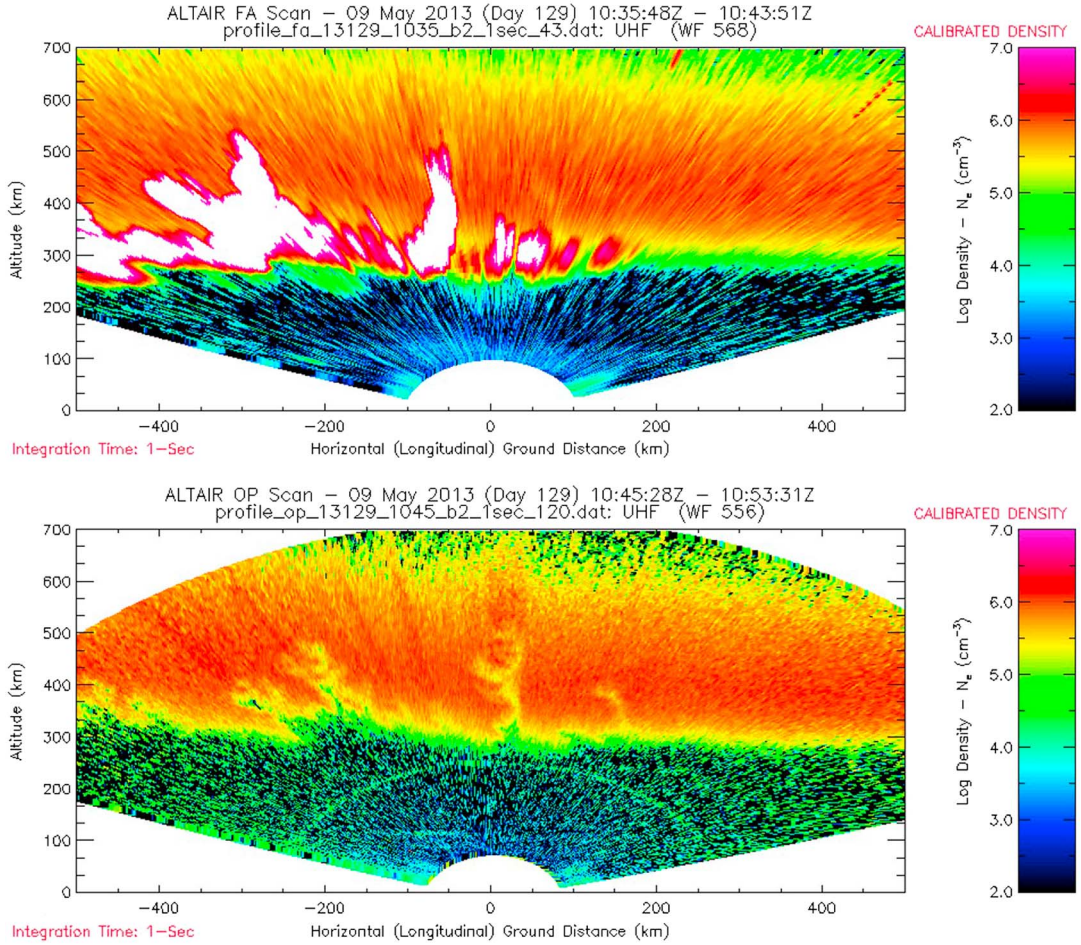

Figure 5. ALTAIR field-aligned (Perp-B) and off-perp scans during MOSC-2.

Figure 6. True color narrow-field camera view of MOSC-1 from Roi-Namur.

Narrow-field imaging spectrographs were deployed on Roi-Namur and Rongelap for examination of the chemical composition of the MOSC clouds. High-sensitivity spectral measurements were made from Roi-Namur with an Acton SP-2156 imaging spectrograph with a 150 mm focal length and micrometer-controlled slit. The sensor was manually operated and repositioned while tracking the cloud making calibration difficult, but initial analyses have allowed for the identification of a number of spectral lines. Sample spectra from MOSC-2 are displayed in Figure 7. Immediately following the release, very strong line emissions in the blue region of the spectrum were observed along with discernable lines in the red region, which begin to dominate the spectrum after ~1 min. Emissions in the violet region represent transition states of Sm^+; however, additional work is required to provide a one-to-one match of the measured and modeled spectra. Prior to the MOSC experiment, the spectrum of SmO^+ was unknown. It is hoped that the elimination of known spectral emissions from Sm, Sm^+, and SmO from these data sets will reveal the spectral components of SmO^+. *Holmes et al.* [2017] provides a more detailed analysis of the high-resolution spectra captured during the MOSC samarium releases.

3.4. Beacon Sensors

A total of nine beacon receivers were fielded at five locations including three different receiver types, each capable of monitoring the CERTO rocket beacons as well as recording data during overflights of Low-Earth Orbiting (LEO) satellites including the AFRL Communication/Navigation Outage Forecasting System satellite [*de la Beaujardière et al.*, 2004]. Phase measurements at 150.012/400.032 MHz for MOSC-1 and 149.988/399.968 MHz for MOSC-2, after accounting for the rocket spin, allowed for the use of the differential phase technique described by *Bernhardt and Siefring* [2006] providing a method for the computation of the integrated TEC along the line of sight to the rocket. On the left in Figure 8, uncorrected TEC data are presented from three receivers sites during MOSC-1, Rongelap, Likiep, and Roi-Namur. Notice the slight bump in TEC recorded at each site coincident to the release at ~159 s into the flight. On the right, the spin-adjusted TEC measurements are presented from the receiver located on Rongelap Atoll indicating enhancements of up to 5 total electron content unit (TECU, 1 TECU = 10^{16} el m^{-2}) from the MOSC-2 cloud and ~4 TECU from MOSC-1. The enhanced TEC values reported from the beacon observations when compared with those determined by integration of the plasma density measurements from ALTAIR (<2 TECU) are consistent with the fact that the radar derived values may be underestimated due to the line of sight during raster scanning and due to the size of the plasma cloud not filling the beam during the first ~100 s after release.

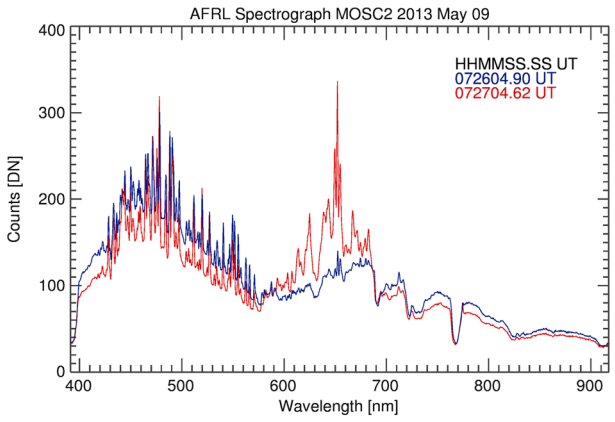

Figure 7. Spectra from MOSC-2 immediately after (blue) and 1 min after (red) release produced by averaging the central 200 pixels in the spatial dimension of the acquired 1340 × 400 images.

3.5. C/NOFS

The timing of the MOSC experiment window proved fortunate as a series of high-elevation overflights of the C/NOFS satellite occurred nightly beginning 26 April 2013. During MOSC-1, a C/NOFS overflight reaching an elevation of ~80° from Roi-Namur began 31 min after launch. Lift-off of MOSC-2, on 9 May 2013, coincided with a C/NOFS pass reaching ~50° elevation beginning just

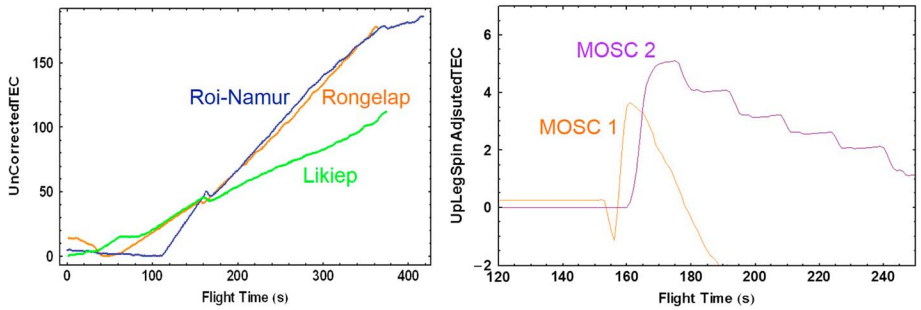

Figure 8. Uncorrected CERTO Beacon TEC measurements from MOSC-1 observed from (left) three ground sites and spin-corrected TEC from (right) MOSC-1 and MOSC-2 from Rongelap.

3 min after launch. Doppler signatures of the beacon on the MOSC-2 rocket and the C/NOFS CERTO beacon were captured in a recording from a GNU Radio Beacon Receiver [*Yamamoto*, 2008] on Roi-Namur. The subsequent C/NOFS pass, ~90 min after launch, occurred directly overhead. Universal Software Radio Peripheral (USRP)-based raw recorders recorded the C/NOFS overflights from Roi-Namur and Rongelap and will be crucial to understanding the direct interaction of the MOSC cloud with the background ionosphere.

In situ sensors on board the C/NOFS satellite include a Vector Electric Field Instrument (VEFI), a planar Langmuir probe (PLP), an ion velocity meter (IVM), and a neutral density meter [*de La Beaujardière et al*., 2004]. Data from the evening of the MOSC-1 launch showed evidence of an extremely turbulent ionosphere. Large depletions over the Pacific were observed with scale sizes of ~4800 km estimated from the zonal extent of the density perturbations observed from PLP (Figure 9, bottom left). Strong upward drifts (Figure 9, middle left) were measured over the Kwajalein sector at ~08:15 UT coincident with strong scintillation activity on local Scintillation Network Decision Aid (SCINDA) sensors. PLP and IVM data from this pass are shown in Figure 9 (left column), while the VEFI electric field data (not shown) indicated eastward ion drifts of 60–120 m/s in the vicinity of Kwajalein Atoll.

When compared with conditions observed during MOSC-1, in situ data from a C/NOFS overflight approximately 1.5 h after the MOSC-2 release shows a significantly less active ionosphere (Figure 9, right column). Small plumes are evident in PLP data (Figure 9, bottom right) with VEFI reporting eastward drifts of ~90 m/s (not shown). Subsequent passes from C/NOFS (~10:56 UT, ~12:39 UT, and ~14:21 UT, not presented here) showed evidence of strong turbulence to the west of the Kwajalein sector. VEFI data were not available during these later passes.

3.6. Digisonde Portable Sounder and HF Propagation

Prior to the MOSC flight experiment, an existing Digisonde Portable Sounder (DPS), installed on Roi-Namur during the 2004 EQUIS II rocket campaign [*Hysell et al*., 2005; *Friedrich et al*., 2006], was upgraded to a DPS-4D [*Reinisch et al*., 2009] capable of synchronizing with a second DPS-4D deployed on Rongelap Atoll for oblique ionospheric soundings. The synchronized DPS-4D systems were used to provide direct estimates of the peak plasma densities from and range to the artificially generated plasma clouds resulting from two MOSC releases.

Ionosonde scheduling during MOSC-1 was optimized based on anticipated plasma density estimates of 10^9 cm^{-3} from theory and earlier modeling studies [*Williams et al*., 2004]. As a result of the lower than anticipated densities achieved during the experiment, poor signal-to-noise levels were reported in the frequency range where the actual cloud density levels appeared leaving a relatively small number of measurements. Based on these results, coordinated soundings for MOSC-2 were further optimized providing higher-resolution observations. Effects from the MOSC-2 cloud were evident in ionograms up to ~45 min after release. In Figure 10, DPS-4D data during MOSC-2 were manually inverted to determine peak plasma densities of up to ~9 MHz.

In 1990, as part of the NICARE 2 experiment, a single HF transmitter/receiver pair was deployed in the Republic of the Marshall Islands to explore the effects of a modified ionosphere on HF propagation links [*Fitzgerald et al*., 1997]. For MOSC, an extensive network of 100 kHz s^{-1} chirp HF transmitters and receivers

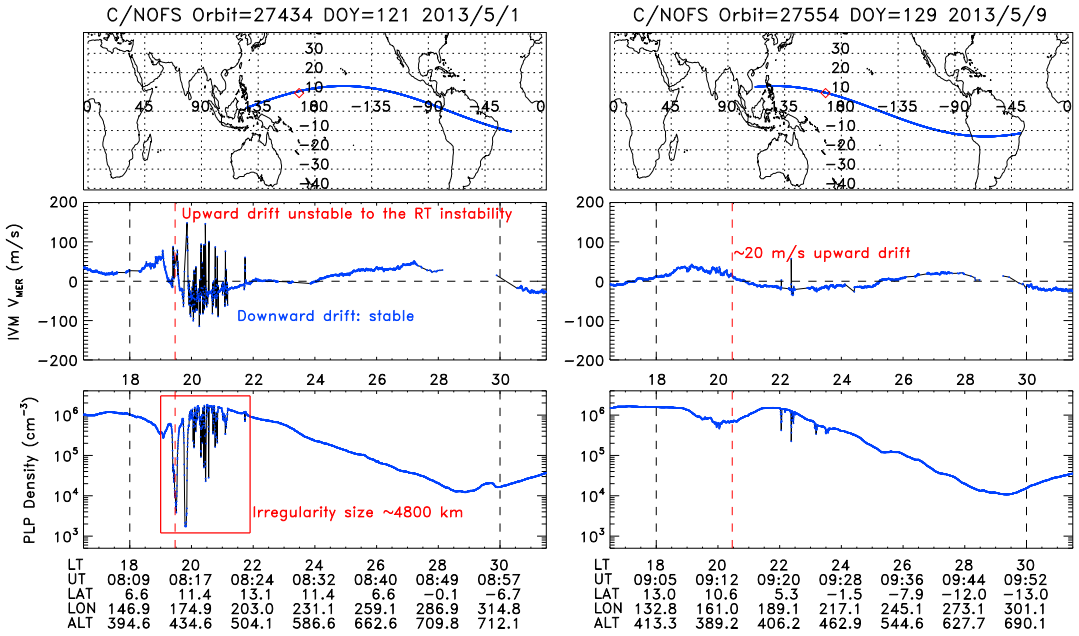

Figure 9. C/NOFS in situ observations during (left column) MOSC-1 and (right column) MOSC-2. (top row) The blue line represents the C/NOFS satellite orbit as a function of geographic latitude and longitude, while the red diamond represents the location of Kwajalein. (middle row) Meridional drift velocities obtained from IVM are displayed as a function of local time, where the positive values indicate upward drifts at low magnetic latitudes. (bottom row) The electron densities obtained from PLP are shown with corresponding local time, universal time, latitude, longitude, and altitude on the *x* axis. The vertical black dashed lines denote 18 and 06 LT, respectively, while the red dashed line represents the longitude of Kwajalein.

enhanced by direction finding capabilities on Kwajalein Island were deployed at five locations. The network provided both north-south and east-west propagation geometries with great circle ranges of more than 300 km [*Jackson-Booth et al.*, 2014]. The instrument configuration is shown in Figure 1 with the dashed lines representing the direct propagation paths between the Wotho, Rongelap, Likiep, Roi-Namur, and Kwajalein sites. Distances between the transmitter/receiver pairs varied from 83 km between Roi-Namur and Kwajalein to 358 km between Wotho and Likiep.

The oblique HF results are illustrated in a series of ionograms recorded on Wotho Atoll from transmitters located on Rongelap Atoll and Likiep Atoll. A 5 min duration transmission sweep started 3 min prior to the launch of MOSC-2 on 9 May 2013 (Figures 11a and 12b) and a further sweep seconds after ignition of the Sm canisters (Figures 11c and 11d). In the latter, a new MOSC layer is evident on both paths at frequencies >10 MHz, together with an "*F* region ghost echo" due to refraction off the MOSC cloud, Figure 12. A more detailed discussion of the results from this portion of the experiment along with modeling analysis of the propagation path can be found in *Joshi et al.* [2017].

3.7. Scintillation and TEC Receivers

As a supplement to the VHF/GPS scintillation and TEC receivers operating on Roi-Namur since 2005 as part of the AFRL Scintillation Network Decision Aid (SCINDA) [*Groves et al.*, 1997; *Caton et al.*, 2004], additional sensors were deployed to the four remaining MOSC ground sites. Nightly monitoring of scintillation activity on geosynchronous VHF links with USRP-based recorders was key to understanding the night-to-night ionospheric dynamics throughout the campaign. Summary scintillation statistics, decorrelation time measurements, and ionospheric drifts from evenings bracketing the two MOSC launch dates are shown in Figure 13. The 1 min scintillation index (S_4, the normalized standard deviation of the intensity measured on the VHF link) is shown in Figures 13a–13c for the evenings before, during, and after each launch. The decorrelation time (τ_i), defined as the point at which an autocorrelation of the intensity reaches one half, provides an indication of the temporal variation of the fluctuations. The ionospheric drift velocity is computed from spaced antenna measurements and shown in Figures 13d–13f. Shaded regions represent the times of sunset and sunrise at 300 km on the link to the geosynchronous satellite. Note the strong scintillation activity

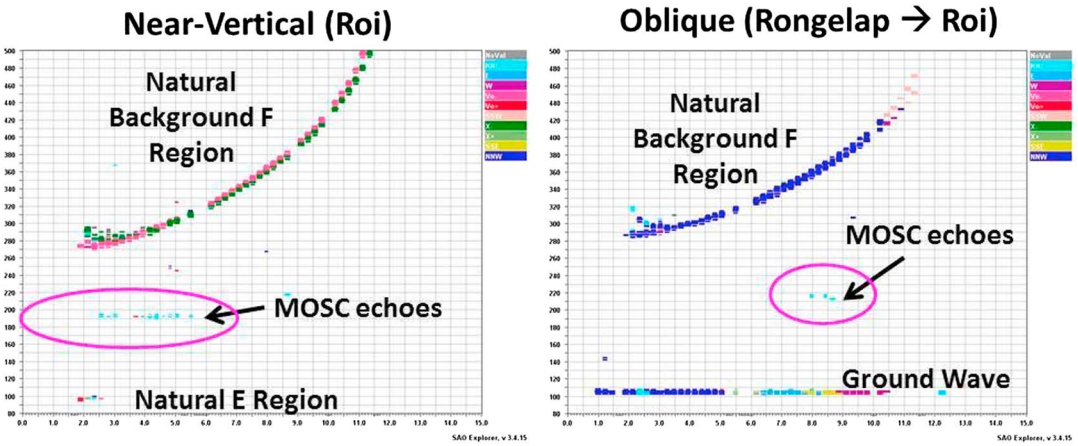

Figure 10. Vertical and oblique DPS-4D observations from MOSC-2.

beginning at sunset on the evening on MOSC-1, 1 May 2013, and the early morning scintillation with the drift velocity turning negative (westward).

NovAtel GSV4004B receivers at each MOSC site recorded 50 Hz raw data and 1 min statistical parameters (S_4, σ_{phi}, and TEC) on GPS links [*Van Dierendonck et al.*, 1993; *Morrissey et al.*, 2004]. Unfortunately, due to the limited availability of ground locations within the Republic of the Marshall Islands, no direct GPS links through the cloud were captured during the flight experiments.

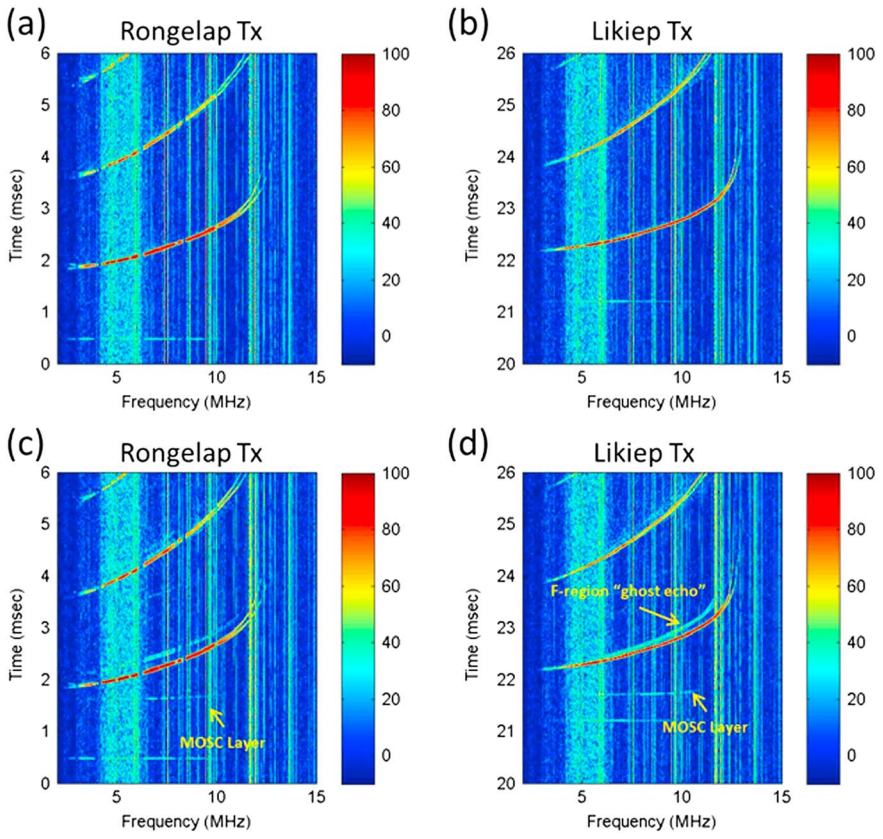

Figure 11. Wotho Atoll ionograms during MOSC-2 from (a and c) Rongelap Atoll and (b and d) Likiep Atoll. Note that the Likiep group delay is offset by 20 ms.

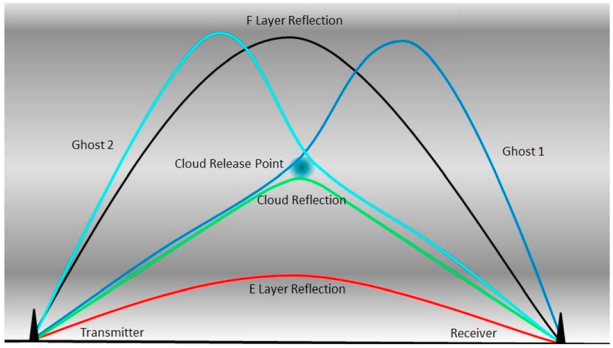

Figure 12. Analysis of anomalous HF returns during the MOSC experiment, "ghost echoes."

3.8. VHF Coherent Scatter Radar

Launch facilities on Kwajalein Atoll during MOSC were shared with a NASA sponsored mission led by the University of Illinois and Clemson University. As part of the Equatorial Vortex Experiment, researchers from the University of Illinois' Electrical and Computer Engineering department installed a VHF coherent backscatter radar on Roi-Namur. Known as the Illinois Radar Interferometer System (IRIS), the system was designed to focus on signatures of *E* region turbulent structures at sunset as potential precursors to nighttime *F* region instabilities. IRIS operated throughout the experiment window, including the evenings of the MOSC launches. Weak backscatter signatures on IRIS in the presence of ionospheric *F* region irregularities during the evening of MOSC-2 were noticeably different than those observed throughout the remainder of the campaign window as demonstrated by the pair of range-time-intensity plots shown in Figure 14. The considerably weaker returns on 9 May 2013 (Figure 14a) as compared with those from the following evening (Figure 14b), more typical of events observed during the campaign, are suggestive of a direct influence of the Sm cloud on the ambient ionosphere. While incoherent scatter returns on ALTAIR showed well developed density depletions in the *F* region at altitudes up to ~500 km (see Figure 5), the 3 m scale structure within the depletions was visibly suppressed in response to the underlying samarium-induced cloud which showed evidence of a slow zonal drift remaining in the same longitude sector for a number of hours. This evidence appears to support a theory that the increased conductivity within the cloud "shorts the polarization fields of small-scale structures to prevent their growth on the gradients of larger scale structures convecting zonally from regions unaffected by the cloud" (E. Kudeki, personal communication, 2013). This interaction between the cloud and the background plasma is a key ingredient for the potential use of this technology to quench development of naturally occurring ionospheric irregularities driven by the *R-T* instability.

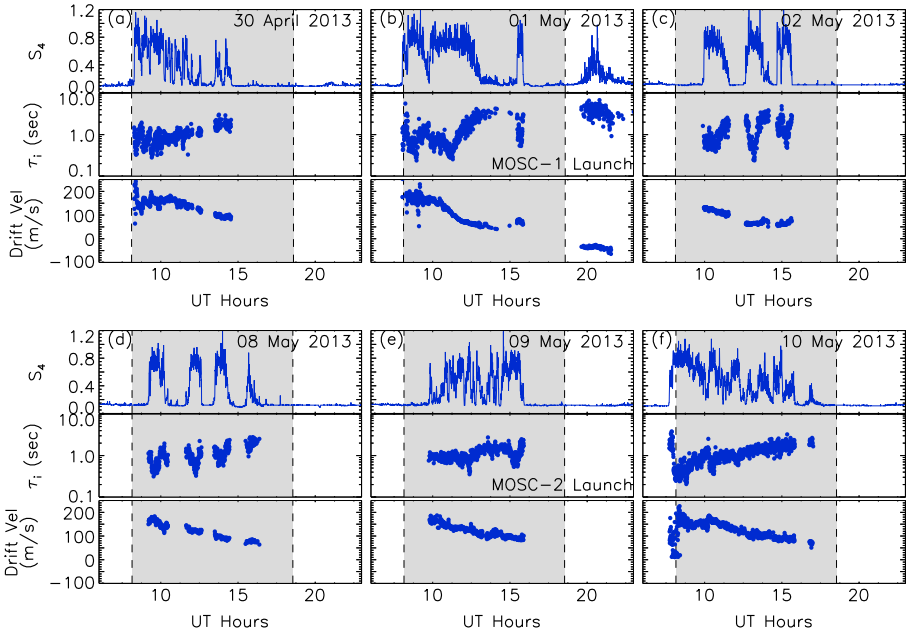

Figure 13. Nightly VHF scintillation observations bracketing the MOSC launches: (a) 30 April, (b) 1 May, and (c) 2 May 2013, (d) 8 May, (e) 9 May, and (f) 10 May 2013.

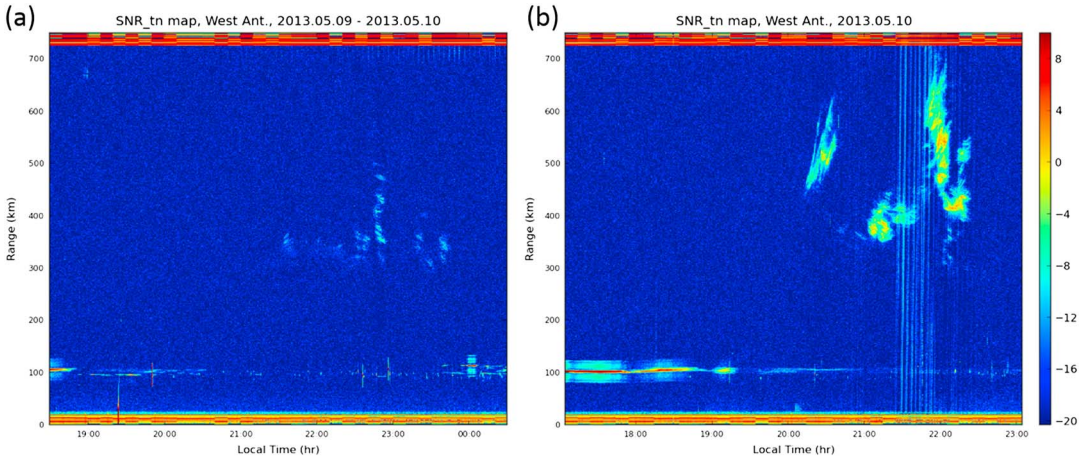

Figure 14. Range-time-intensity plots from the Illinois Radar Interferometer System (IRIS) during (a) the evening of MOSC-2 and (b) a typical evening during the campaign.

4. Initial Results

4.1. MOSC Cloud Model

The primary objective of the 2013 MOSC experiment was a comprehensive diagnosis of the artificially generated plasma cloud resulting from release of Sm vapor in the upper atmosphere and the development of a Sm plasma cloud model. Optical data from an all-sky imager on Roi-Namur near the launch site captured 180° field-of-view images at six wavelengths each minute providing location and spatial scale of the cloud. During early development, the ALTAIR radar tracked the cloud in a raster scanning mode providing line-of-sight plasma density measurements via incoherent scatter at VHF and UHF frequencies. Pointing locations for ALTAIR during MOSC-2 are highlighted in Figure 15 as cross hairs within the cloud against a background of green line (5577 Å) emissions in 2 min intervals. Merging the line-of-sight density measurements from the radar with optical observations and fitting these data with a 2-D Gaussian distribution provides a quantitative model defining the cloud location, widths in two dimensions, and rotation relative to the coordinate axes. A snapshot of the observed irradiance at 6300 Å and Gaussian modeled cloud dimensions several minutes after release of the MOSC-2 cloud is shown in Figure 16. A comparison of modeled TEC values from ALTAIR radar observations for ~30 min from the MOSC-1 launch on 1 May 2013 is shown in Figure 17. MOSC optical data recorded during both launches exhibited a linear expansion of the cloud with time. Assuming this expansion was similar in the vertical direction, which is not directly observable with optics from the launch site, suggests that cloud densities should have decreased with time as t^{-3} even if no recombination or loss of the plasma occurred. Prior to the MOSC experiment, the most reliable chemical release model published, the barium ionization and expansion model of *Ma and Schunk* [1993], predicts a $t^{-3/2}$ dependence.

A closer examination of the time dependence of the peak densities achieved from MOSC-2 is shown in Figure 18. Here peak plasma densities as observed from near vertical soundings from the DPS-4D on Roi-Namur are shown (green) and fit with a curve (blue) along with density measurements of the cloud from ALTAIR (red) captured in a raster scanning mode. As would be expected, since the radar line of sight only occasionally passes through the center of the cloud, the fit to the DPS-4D data serves as an upper bound on the ALTAIR data. The best fit line to the soundings has an exponent between −0.67 and −0.8, well below the −1.5 exponent expected from diffusive spreading of a cloud with a constant number of ions and even farther below the t^{-3} density dependence that would be inferred from the observed linear optical spread of the clouds and an assumption of constant ion number. Given the strong correlation between the radar plasma densities and the optics-based model, the most reasonable conclusion that can be drawn from these findings is that ionization continued to be added to the cloud as a function of time, preventing densities from dropping as rapidly as they would under diffusive spreading. The slow (much slower than linear geometric expansion of a cloud with constant particle number) decay of the cloud density is a benefit for possible applications as significant density was still present up to 1 h after release. A more detailed description of the MOSC

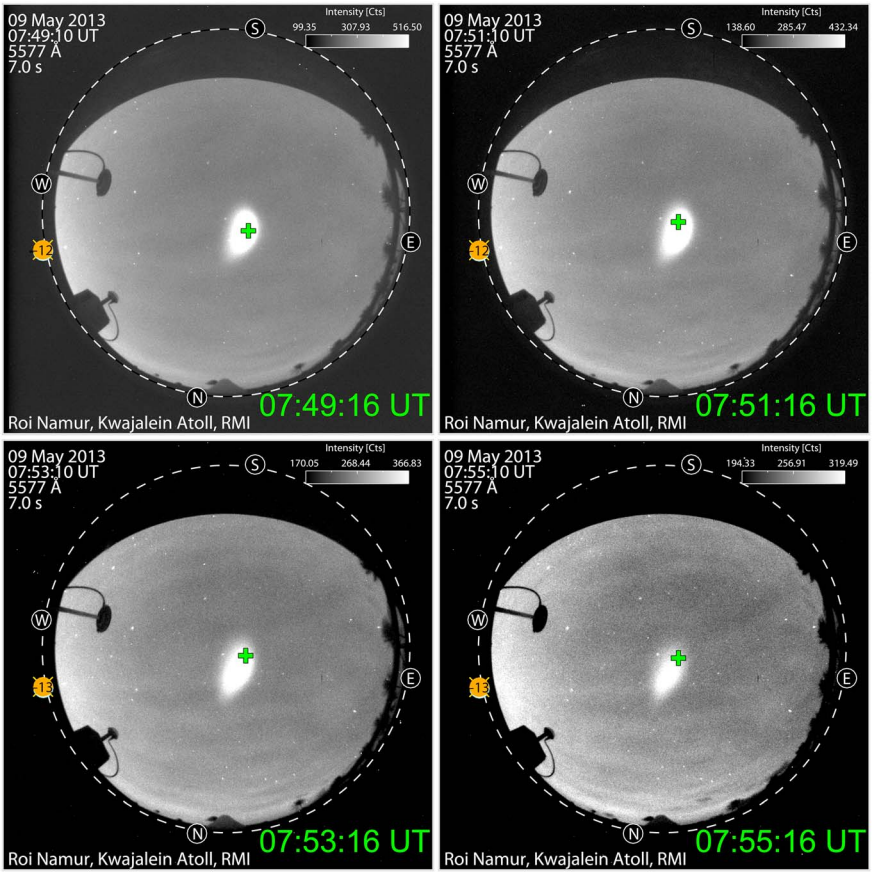

Figure 15. All-sky images and ALTAIR Tracking Information during MOSC-2. Cross hairs indicate ALTAIR pointing during image capture.

cloud model can be found in T. R. Pedersen et al. (Empirical modeling of plasma clouds produced by the Metal Oxide Space Cloud (MOSC) experiment, *Radio Science*, in review, 2016)

4.2. MOSC Chemistry Analysis

Concurrent with analyses of ground diagnostics collected during the two MOSC releases, a detailed investigation of samarium chemistry was conducted to help explain the unanticipated results. As described by *Cox et al.* [2015], a laboratory investigation of the ion-molecule chemistry of SmO^+ and Sm^+ focused on the likely

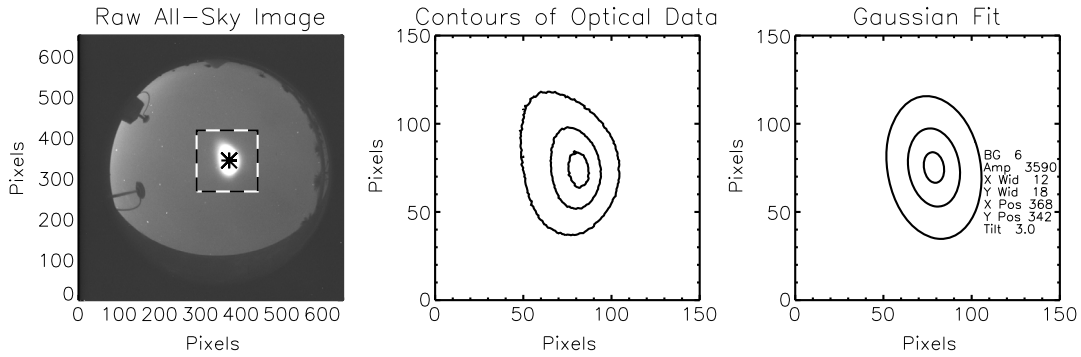

Figure 16. (left) Two-dimensional Gaussian model fits to the MOSC-2 cloud at 630.0 nm with the region of interest highlighted with a dashed outline and the radar beam position at the time marked with an asterisk. (middle and right) Contours of image intensity and contours from the 2-D Gaussian fit to the intensity.

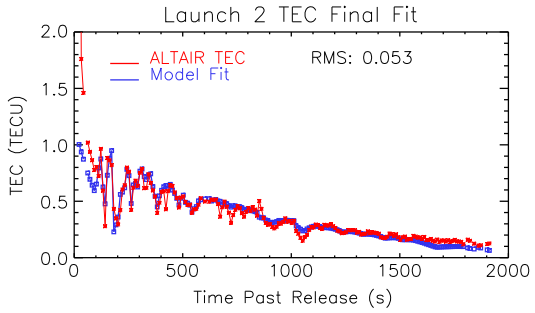

Figure 17. TEC comparison from the MOSC Cloud Model (blue) and ALTAIR (red) during MOSC-1.

evolution of these species in the ambient atmosphere near ~200 km. In brief, any Sm^+ formed via photoionization will quickly react with molecular oxygen to yield SmO^+, while SmO^+ will be inert to further reaction. Importantly, these ions will not react to form ions such as SmO_2^+, which would act as an electron density sink by readily recombining with electrons.

Results of these experiments have raised questions regarding literature reporting on the exothermicity of the reaction between Sm and ambient oxygen ($Sm + O \rightarrow SmO^+ + e$), previously specified as $\Delta H_r^o = -0.35 \pm 0.1$ eV [*Brewer and Rosenblatt*, 1969]. The bond strength of SmO^+ and the ionization energy of SmO were reevaluated, and the exothermicity of this reaction was corrected to the substantially lower value of $\Delta H_r^o = -0.08 \pm 0.07$ eV [*Cox et al.*, 2015]. This revision has potentially large effects on the expected stability of SmO^+ at 200 km. Electrons with >0.08 eV translational energy can drive the reverse reaction resulting in dissociative recombination of SmO^+. Figure 19 shows an approximate energy distribution of electrons at 200 km, with shaded areas denoting the fraction of the population exceeding the previously believed exothermicity of the reaction (red) and the much larger population (blue plus red) exceeding the revised value. The importance of this revision hinges on the currently unknown rate of reaction of the dissociative recombination of SmO^+. Plans to make this measurement using the Heidelberg Test Storage Ring for heavy ions at the University of Heidelberg [*Habs et al.*, 1989], the only capable facility, are in progress. Meanwhile, estimates of the rate suggest that at 200 km, an equilibrium between $Sm + O \rightarrow SmO^+ + e$ and its reverse reaction will be established, limiting ionization to on the order of 10% of the released quantity of Sm [*Cox et al.*, 2015].

Experiments directly measuring the rate coefficient of the chemi-ionization reaction as a function of temperature have been recently completed at AFRL [*Ard et al.*, 2015]. The measurements indicate that the reaction of Sm with O is in line with previous estimates and increases with temperature. The data also indicate but do not prove that excited states of Sm react more rapidly, which complicates modeling of these systems and points to the need for future experiments. Including in the results was the kinetics of analogous reactions with Nd, which does not suffer from the potential deleterious effects of rapid reverse reaction. That reaction proceeded at the collisional value. Future experiments will look at other metals and oxidizers other than atomic oxygen, allowing for increased flexibility in creating advantageous chemical release conditions.

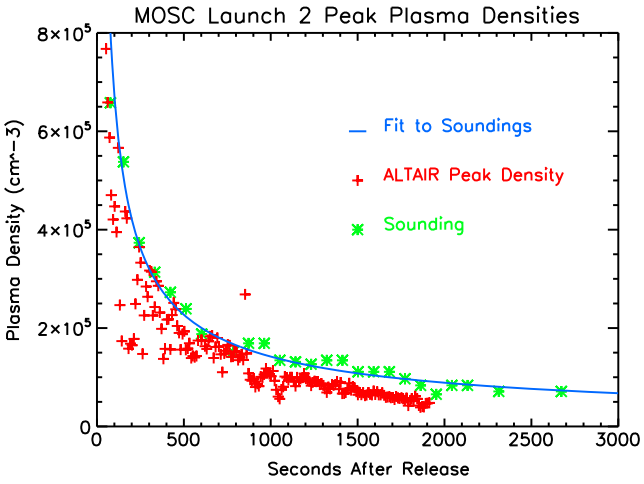

Figure 18. Comparison of the MOSC-2 peak plasma densities from DPS-4D and ALTAIR.

In a related study submitted as a companion article to this review, *Bernhardt et al.* [2017] present a comprehensive analysis of Sm atom energy levels and possible transition states coupled to neutral and ion transport as well as ion-electron and ion-neutral chemical reactions. Sm atomic and molecular ion plasma densities from the Samarium Release Code (SaReC), which is a theoretical model designed by the Naval Research Laboratory to study the MOSC experiment, are shown in Figure 20. The SaReC model includes

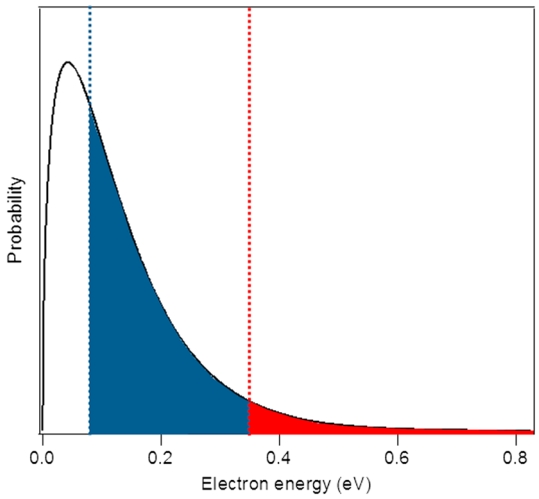

Figure 19. Electron energy distribution at 200 km with $T = 1000$ K (reprinted with permission from *J. Chem. Phys.* 142, 134307 Copyright 2015, AIP Publishing LLC).

the effects of neutral cloud reaction with atomic oxygen, photo-ionization by sunlight, dissociative recombination of molecular ions, diffusive expansion, and optical emissions by solar pumped excited states. The outputs from SaReC are compared to radar, ionosonde, radio beacon, and optical spectra measured during the MOSC releases by *Bernhardt et al.* [2017]. The main conclusion of this theoretical study is that dissociative recombination of the SmO^+ ion with electrons is the primary process that limits the cloud lifetime.

4.3. Ionospheric Modeling and Simulations

Prior to launch, the Spacecraft/Orbiter Contamination Representation Accounting for Transiently Emitted Species model [*Elgin et al.*, 1990] was exercised to describe the temporal evolution of a samarium vapor cloud and used in conjunction with an ambipolar diffusion model incorporating both photoionization and chemi-ionization reaction rates for Sm + O providing estimated density contours of the MOSC cloud as a function of time [*Williams et al.*, 2004]. Output from this modeling effort was applied to the physics-based model (PBMOD) [*Retterer*, 2010] in an attempt to analyze potential effects of the plasma cloud on the background ionosphere. Results from PBMOD simulations with an injection of 5 kg of plasma at an altitude of 200 km (mapping to an apex height of ~250 km) in the longitude sector of Kwajalein Atoll showed the development of a hook-like signature in the bottomside of the *F* region as seen in a plot of ionospheric conductance as a function of apex altitude on the left in Figure 21. Although, based on ground observations, only an estimated ~10% of the Sm released during MOSC was ionized, the hook-type signature was observed in ALTAIR zonal FA scans during both MOSC-1 and MOSC-2.

In a companion paper submitted with this experimental overview, the actual cloud characteristics as defined by the MOSC Cloud Model are used to drive more realistic PBMOD simulations [*Retterer et al.*, 2017]. Such investigation will provide information regarding the potential for use of this technology in the suppression of naturally occurring ionospheric scintillation. Largely driven by the Rayleigh-Taylor instability (RTI), ionospheric irregularities in the nighttime equatorial region cause routine disruptions on transionospheric communication including UHF SATCOM and GPS navigation [*Kelley et al.*, 2011; *Makela et al.*, 2006]. The exponential growth rate of the RTI can be shown to be inversely proportional to the *E* region conductivity (Σ_E) which is rapidly quenched at dusk due to the lack of solar production [*Sultan*, 1996]. At question is whether the increase of Σ_E through artificial means can suppress the drivers of RTI through the shorting out local electric fields, thus providing assurance of clear communications for an extended period of time. Is the chemi-ionization potential of the Sm reaction suitable to provide a long-lasting cloud for scintillation suppression? If so, what amount of material would be necessary to achieve the desired results? Might cloud-shaping be required to produce optimal effects over a sizable region?

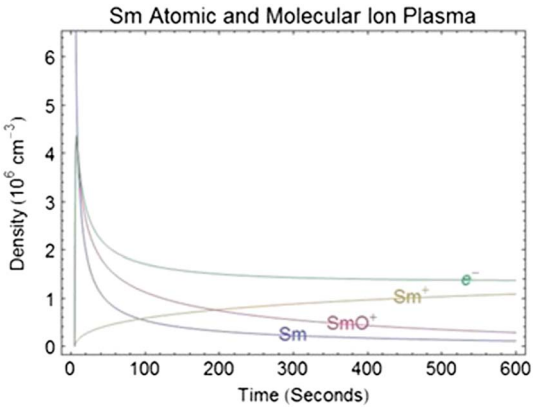

Figure 20. Sm atomic and molecular ion density from the SaReC model.

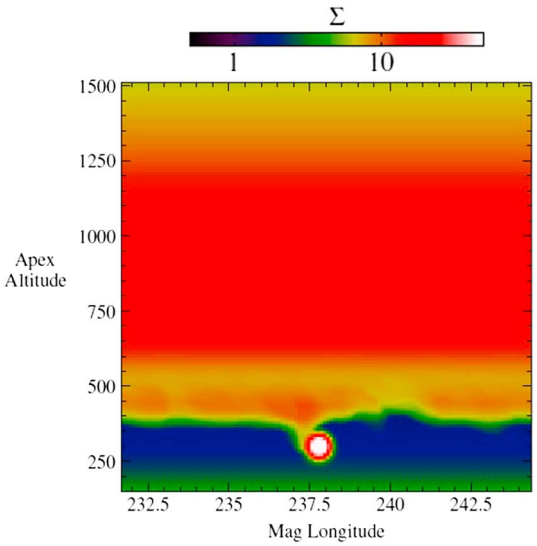

Figure 21. PBMOD estimates of ionospheric conductance for a fully ionized release of 10 kg of Sm at an apex altitude near 250 km.

Are alternate materials available that would provide better opportunities for results?

4.4. Cloud Morphology

As can be seen in all-sky images captured during the experiment, the behavior of the visible MOSC-1 cloud was remarkably different from that of MOSC-2. The images presented in Figure 22 were taken minutes after each release. While the MOSC-2 cloud followed the anticipated pattern with an extension of the optical cloud primarily in the north-south direction along the magnetic field lines, the MOSC-1 cloud is elongated east-west direction across field lines. Although we do not have a conclusive answer to explain these differences, the disturbed geomagnetic conditions present during MOSC-1 resulted in dramatically different background conditions compared with MOSC-2. Presumably, significantly larger neutral and plasma drifts during MOSC-1 could have resulted in a differential east-west motion between the neutral and ion clouds which would have the effect of stretching the optical cloud perpendicular to the field lines. The MOSC-1 cloud drifted slowly eastward in its early development rapidly turning westward with an estimated velocity of ~140 m/s while growing into an ellipsoid with an elongated meridional axis. Conversely, the MOSC-2 cloud drifted toward the southeast for a period of minutes then turned slowly westward while becoming oblong with the major axis in the zonal direction.

Figure 23 shows data recorded by the DMSP F18 satellite in Sun-synchronous orbit near 20:00 LT at ~860 km on the evenings of 1 and 9 May 2013 approximately 1:45 after the MOSC-1 and MOSC-2 releases (solid lines). Dotted lines in Figures 23a–23c present data observed during the previous orbit prior to the substorm onset near 07:30 UT. Note the dramatic difference between the plasma parameters before and after substorm onset as well as those between the two evenings. The enhanced and highly structured density and vertical/eastward velocities observed on 1 May (Figures 23a–23c) suggest that the ionosphere was uplifted and subjected to plasma instabilities presumably due to the presence of an enhanced (penetration) electric field. In contrast, the ionosphere represented in Figures 23a′–23c′ during the MOSC-2 launch, both the density and velocities are relatively smooth. The discrete values demonstrated in Figure 23b′, where the

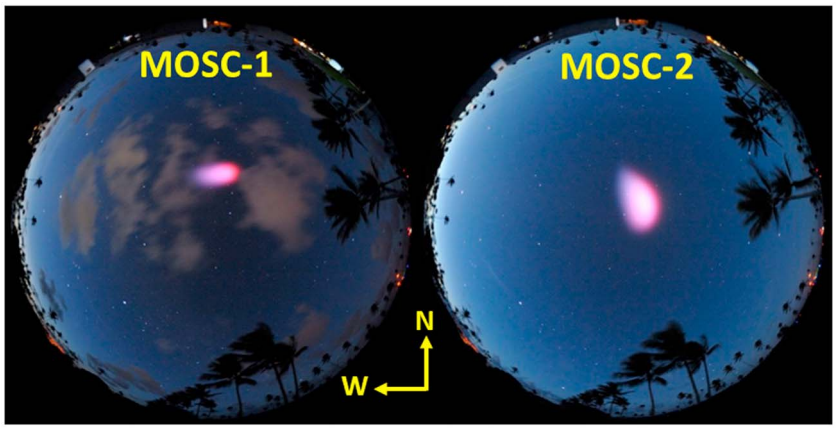

Figure 22. Real-color all-sky images of the MOSC clouds (courtesy of Clemson University).

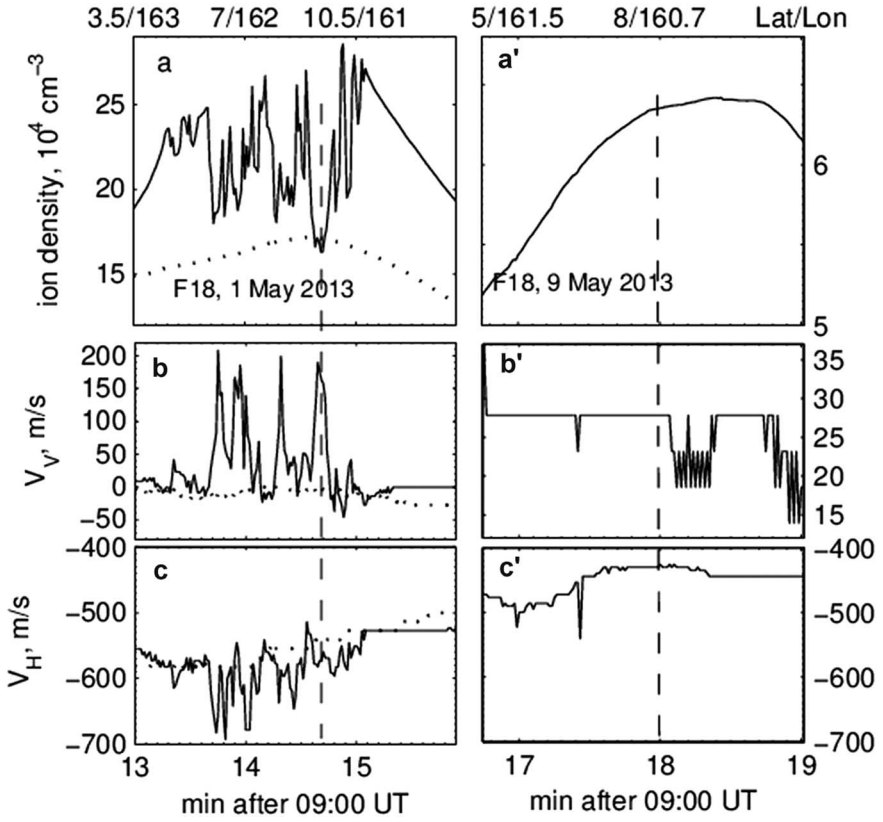

Figure 23. Measurements from DMSP F18 on the evenings of (a–c) 1 May 2013 (left) and (a′–c′) 9 May 2013. Variations of the ion density (a and a′), vertical (b and b′), and horizontal (c and c′, positive westward) velocities along the satellite orbit. The geographic latitudes and longitudes are listed on top. Dotted lines in Figures 23a–23c represent observations during the previous orbit at ~20° in longitude to the east and ~90 min earlier. Dashed vertical lines indicate the time of the crossing of the MOSC cloud's geographic latitudes.

vertical scale is much reduced as compared with Figure 23b, are representative of the instrument sensitivity and a 1 s smoothed averaging performed on the raw 12 Hz velocity observations.

5. Summary

The Metal Oxide Space Cloud (MOSC) sounding rocket experiment was successfully executed in May 2013 resulting in the first comprehensive diagnosis of an artificially generated plasma cloud from the release of samarium (Sm) vapor in the upper atmosphere. Two Terrier MK70-Improved Orion suborbital sounding rockets were launched from the Speedball complex on Roi-Namur at the Kwajalein Missile Range near dusk on separate evenings (1 and 9 May 2013) carrying payloads consisting of Sm canisters and two-frequency beacons. Preset timers on each rocket triggered the release of atomized Sm at select altitudes. The resulting plasma clouds were probed by more than three dozen instruments deployed at five locations in the Republic of the Marshall Islands including incoherent scatter measurements with the Advanced Research Project Agency (ARPA) Long-Range Tracking and Instrumentation Radar (ALTAIR). Detailed analyses of data from multiple sensors resulted in the development of the MOSC Cloud Model which is currently being used in conjunction with ionospheric propagation models to examine the potential impacts of artificial ionospheric clouds on radio wave propagation and the potential for assured communications through the suppression of naturally occurring ionospheric scintillation. Experimental findings during MOSC provided the motivation for advanced studies into the chemical properties of lanthanide metals providing a new and better understanding of their chemi-ionization properties. While this paper serves as a high-level overview of the experiment, interested readers may find more detailed descriptions of the various aspects of MOSC in a series of articles submitted as companion pieces to this manuscript.

Appendix A

Ground instrumentation for the 2013 MOSC experiment included installation of diagnostic equipment on five islands and four atolls in the Republic of the Marshall Islands. Table A1 provides detailed listing of the experimental sensors providing data for postflight analysis of the MOSC plasma clouds.

Table A1. Experimental Instrumentation for the 2013 MOSC Experiment

Site	Source	Instrument
Kwajalein Island, Kwajalein Atoll	AFRL	USRP raw recorder beacon Rx
	AFRL	NovAtel GPS scintillation/TEC Rx
	UK	18 channel N-IRIS HF Rx
	USAKA	Tracking radar for sounding rocket
	NRL	Tri-Band Beacon Rx
Roi-Namur Island, Kwajalein Atoll	AFRL	USRP raw recorder beacon Rx
	AFRL	Tri-Band Beacon Receiver
	AFRL	GNU radio beacon receiver (dual band)
	AFRL	USRP SCINDA VHF scintillation Rx
	AFRL	Narrowband VHF scintillation receiver
	AFRL	NovAtel GPS scintillation/TEC receiver
	AFRL	Digisonde portable sounder (DPS-4D)
	AFRL	All-sky imager and narrow-field cameras
	AFRL	Optical spectrograph
	AFRL (via MIT/LL)	HF Rx
	USAKA	ALTAIR
	NASA/SRPO	Ground telemetry
	UK	HF delay Doppler Tx
	UK	HF chirp transmitter
	UK	IRIS HF single channel Rx
	University of Illinois	Illinois Radar Interferometer System (IRIS)—coherent backscatter radar
	Clemson University	Multiple cameras
Wotho Atoll	AFRL	NovAtel GPS scintillation/TEC Rx
	AFRL	USRP SCINDA VHF scintillation Rx
	AFRL (via MIT/LL)	HF Rx
	AFRL	Tri-Band Beacon receiver
	UK	IRIS2 HF receiver
	UK	IRIS2 HF receiver
Rongelap Atoll	AFRL	NovAtel GPS scintillation/TEC Rx
	AFRL	All-sky imager and narrow-field cameras
	AFRL	Optical spectrograph
	AFRL	NovAtel GPS scintillation/TEC Rx
	AFRL	USRP SCINDA VHF scintillation Rx
	AFRL	Digisonde Portable Sounder (DPS-4D)
	AFRL	USRP raw recorder beacon Rx
	UK	Roke X72/1/8922/510 HF Rx (sweep)
	UK	Roke X72/1/8922/510 HF Rx (delay Doppler)
	UK	IRIS2 HF receiver
	Clemson University	Multiple cameras
	AFRL	NovAtel GPS scintillation/TEC Rx
	Clemson University	Multiple cameras
Likiep Atoll	AFRL	NovAtel GPS scintillation/TEC Rx
	AFRL	USRP SCINDA VHF scintillation Rx
	AFRL (via MIT/LL)	HF Rx
	AFRL (via MIT/LL)	HF Tx
	NRL	Tri-Band Beacon Rx
	UK	IRIS2 HF receiver
	UK	Roke X72/1/8922/510 HF Tx (FFPC)
	Clemson University	Multiple cameras

Acknowledgments
The MOSC research team would like to thank the U.S. Department of Defense Space Test Program for their support in providing the launch vehicles and launch support for the MOSC payloads, and the Air Force Office of Scientific Research for supporting data analysis at AFRL. We would also like to offer our appreciation to the to the NASA Sounding Rocket Program and their contract team at Orbital Sciences for their assistance in everything from building and flying the rockets to providing support for the complicated logistics. The AFRL field team included support from Daniel Emmons, Daniel Miller, Brett Stephens, and Eric Sutton. The research at the Naval Research Laboratory was sponsored by the NRL 6.1 Base Program. The UK team would like to thank MOD and the Defence Science and Technology Laboratory for their support in fielding and analyzing data from HF Tx/Rx network. The MOD field team included support from Matthew Angling, Gemma Attril, Graham George, and Stephen White. Requests for access to data collected during the MOSC experiment will be processed on a case-by-case basis pursuant to official Air Force Research Laboratory policy for public release of information.

References

Ard, S. G., N. S. Shuman, O. Martinez Jr., M. T. Brumbach, and A. Viggiano (2015), Kinetics of chemi-ionization reactions of lanthanide metals (Nd, Sm) from 150–450 K, *J. Phys. Chem.*, *143*, 204303, doi:10.1063/1.4934995.

Bernhardt, P. A. (1992), Probing the magnetosphere using chemical releases from the CRRES satellite, *Phys. Fluids B*, *4*, 2249–2256.

Bernhardt, P. A., and C. L. Siefring (2006), New satellite-based systems for ionospheric tomography and scintillation region imaging, *Radio Sci.*, *41*, RS5S23, doi:10.1029/2005RS003360.

Bernhardt, P. A., C. L. Siefring, S. J. Briczinski, A. Viggiano, R. Caton, T. Pedersen, J. Holmes, S. Ard, N. Shuman, and K. Groves (2017), A physics-based model for the ionization of samarium by the MOSC chemical releases in the upper atmosphere, *Radio Sci.*, *52*, doi:10.1002/2016RS006078.

Brewer, L., and G. M. Rosenblatt (1969), Dissociation energies and free energy functions of gaseous monoxides, in *Advances in High Temperature Chemistry*, edited by L. Eyring, 1 pp., Academic, New York.

Çakir, S., G. Haerendel, and J. V. Eccles (1992), Modeling the ionospheric response to artificially produced density enhancements, *J. Geophys. Res.*, *97*, 1193–1207, doi:10.1029/91JA02228.

Cannon, P. S., K. M. Groves, D. J. Fraser, W. J. Donnelly, and K. Perrier (2006), Signal distortion on V/UHF trans-ionospheirc paths: First results from WIDE, *Radio Sci.*, *41*, RS5S40, doi:10.1029/2005RS003369.

Caton, R. G., W. J. McNeil, K. M. Groves, and S. Basu (2004), GPS proxy model for real-time UHF satellite communications scintillation maps from the Scintillation Network Decision Aid (SCINDA), *Radio Sci.*, *39*, RS1S22, doi:10.1029/2002RS002821.

Caton, R. G., C. S. Carrano, C. M. Alcala, K. M. Groves, T. Beach, and D. Sponseller (2009), Simulating the effects of scintillation on transionospheric signals with a two-way phase screen constructed from ALTAIR phase-derived TEC, *Radio Sci.*, *44*, RS0A12, doi:10.1029/2008RS004047.

Cox, R. M., K. JungSoo, P. B. Armentrout, J. Bartlett, R. A. VanGundy, M. C. Heaven, S. G. Ard, J. J. Melko, N. S. Shuman, and A. A. Viggiano (2015), Evaluation of the exothermicity of the chemi-ionization reaction $Sm + O \rightarrow SmO^+ + e^-$, *J. Chem. Phys.*, *142*, 134307, doi:10.1063/1.4916396.

Davis, T. N. (1979), Chemical releases in the ionosphere, *Rep. Prog. Phys.*, *42*, 1565.

de La Beaujardière, O., et al. (2004), C/NOFS: A mission to forecast scintillations, *J. Atmos. Sol. Terr. Phys.*, *66*, 1573–1591, doi:10.1016/j.jastp.2004.07.030.

Edwards, H. D., J. F. Bedinger, E. R. Manring, and C. D. Cooper (1955), Emission from a sodium cloud artificially produced by means of a rocket, in *The Airglow and the Aurorae*, edited by E. B. Armstrong and A. Dalgarno, pp. 122–134, Pergamon, London.

Elgin, J. B., D. C. Cooke, M. F. Tautz, and E. Murad (1990), Modeling of atmospherically induced gas phase optical contamination from orbiting spacecraft, *J. Geophys. Res.*, *95*, 12,197–12,208, doi:10.1029/JA095iA08p12197.

Files, C. W., C. Stokes, and P. Zavitsanos (2007), Exploitation of chemi-ionization for high density plasma generation, Internal AFRL Report on Contract F19628-02-C-0088.

Fitzgerald, T. J., P. E. Argo, and R. C. Carlos (1997), Effects of artificially modified ionospheres on HF propagation: Negative ion cation release experiment 2 and CRRES Coqui experiments, *Radio Sci.*, *32*, 579–591, doi:10.1029/96RS03597.

Friedrich, M., K. M. Torkar, G. A. Lehmacher, C. L. Croskey, J. D. Mitchell, E. Kudeki, and M. Milla (2006), Rocket and incoherent scatter radar common-volume electron measurements of the equatorial lower ionosphere, *Geophys. Res. Lett.*, *33*, L08807, doi:10.1029/2005GL024622.

Giles, B. L., M. A. McCook, M. W. McCook, and G. P. Miller (1995), CRRES Satellite Program, *NASA Tech. Memo. 108494*, June.

Groves, K. M., et al. (1997), Equatorial scintillation and systems support, *Radio Sci.*, *32*, 2047–2064, doi:10.1029/97RS00836.

Habs, D., et al. (1989), First experiments with the Heidelberg test storage ring (TSR), *Nucl. Instrum. Methods*, *43*(3), 390–410.

Heppner, J. P., M. L. Miller, M. B. Pongratz, G. M. Smith, L. L. Smith, S. B. Mende, and N. R. Nath (1981), The cameo barium releases: $E_{\parallel}$ fields over the polar cap, *J. Geophys. Res.*, *86*, 3519–3542, doi:10.1029/JA086iA05p03519.

Holmes, J. M., R. A. Dressler, T. R. Pedersen, R. G. Caton, and D. Miller(2017), A combined spectroscopic and plasma chemical kinetic analysis ofionospheric samarium releases, *Radio Sci.*, *52*, doi:10.1002/2016RS006084.

Huba, J. D., P. A. Bernhardt, and J. G. Lyon (1992), Preliminary study of the CRRES magnetospheric barium releases, *J. Geophys. Res.*, *97*, 11–24, doi:10.1029/91JA02144.

Hunton, D. E., P. J. Wolf, and T. M. Shadid (1998), Ionization mechanisms in CRRES chemical releases: 1. In situ measurements and model results, *J. Geophys. Res.*, *103*, 457–470, doi:10.1029/97JA02344.

Hysell, D. L., M. C. Kelley, W. E. Swartz, and D. T. Farley (1994), VHF radar and rocket observations of equatorial spread *F* on Kwajalein, *J. Geophys. Res.*, *99*, 15,065–15,085, doi:10.1029/94JA00476.

Hysell, D. L., M. F. Larsen, C. M. Swenson, A. Barjatya, T. F. Wheeler, M. F. Sarango, R. F. Woodman, and J. L. Chau (2005), Onset conditions for equatorial spread *F* determined during EQUIS II, *Geophys. Res. Lett.*, *32*, L24104, doi:10.1029/2005GL024743.

Jackson-Booth, N. K., P. S. Cannon, M. M. Bradley, and P. A. Arthur (2012), New oblique sounders for ionospheric research, in *Ionospheric Radio Systems and Techniques*, pp. 1–3, IET, York, U. K.

Jackson-Booth, N. K., P. S. Cannon, M. J. Angling, R. G. Caton, K. M. Groves, T. R. Pedersen, R. T. Parris, and Y.-J. Su (2014), Preliminary HF results from the Metal Oxide Space Cloud (MOSC) experiment, in *General Assembly and Scientific Symposium (URSI GASS), 2014 XXXIth URSI, 16–23 Aug.*, pp. 1–4, Curan Assoc., Redhook, New York, doi:10.1109/URSIGASS.2014.6929958.

Johnson, A. L., and A. M. Hocutt (1984), Scintillation results from ionospheric modification experiment, *Radio Sci.*, *19*, 741–748, doi:10.1029/RS019i003p00741.

Joshi, D., K. Groves, W. McNeil, C. Carrano, R. Caton, R. T. Parris, T. Pedersen, P. Cannon, M. Angling, and N. Jackson-Booth (2017), HF propagation results from the Metal Oxide Space Cloud (MOSC) Experiment, *Radio Sci., 52*, doi:10.1002/2016RS006164.

Kelley, M. C., A. Pedersen, U. V. Fahleson, D. Jones, and D. Köhn (1974), Active experiments stimulating waves and particle precipitation with small ionospheric barium releases, *J. Geophys. Res.*, *79*, 2859–2867, doi:10.1029/JA079i019p02859.

Kelley, M. C., J. J. Makela, O. de La Beaujardière, and J. Retterer (2011), Convective ionospheric storms: A review, *Rev. Geophys.*, *49*, RG2003, doi:10.1029/2010RG000340.

Knepp, D. L., and H. L. F. Houpis (1991), Altair VHF/UHF/observations of multipath and backscatter enhancement, *IEEE Trans. Antennas Propag.*, *AP-39*(4), 528–534.

Kudeki, E., M. Milla, M. Friedrich, G. Lehmacher, and D. Sponseller (2006), ALTAIR incoherent scatter observations of the equatorial daytime ionosphere, *Geophys. Res. Lett.*, *33*, L08108, doi:10.1029/2005GL025180.

Larsen, M. F., I. S. Mikkelsen, J. W. Meriwether, R. Niciejewski, and K. Vickery (1989), Simultaneous observations of neutral winds and electric fields at spaced locations in the dawn auroral oval, *J. Geophys. Res.*, *94*, 17,235–17,243, doi:10.1029/JA094iA12p17235.

Lüst, R. (2001), Barium cloud experiments in the upper atmosphere, in *The Century of Space Science*, edited by J. A. M. Bleeker, J. Geiss, and M. C. E. Huber, pp. 179–187, Kluwer Acad., Amsterdam.

Ma, T.-Z., and R. W. Schunk (1993), Ionization and expansion of barium clouds in the ionosphere, *J. Geophys. Res.*, *98*, 323–336, doi:10.1029/92JA01552.

Makela, J. J., M. C. Kelley, and O. de la Beaujardiére (2006), Convective ionospheric storms: A major space weather problem, *Space Weather*, *4*, S02C04, doi:10.1029/2005SW000144.

Mendillo, M., J. Baumgardner, X. Pi, P. J. Sultan, and R. Tsunoda (1992), Onset conditions for equatorial spread *F*, *J. Geophys. Res.*, *97*, 13,865–13,876, doi:10.1029/92JA00647.

Milinevsky, G. P., A. I. Kashirin, Y. A. Romanovsky, H. C. Sgtenbaek-Nielsen, and M. C. Kelley (1993), Long-lived artificial ion clouds in the Earth's ionosphere, *Geophys. Res. Lett.*, *20*, 1019–1022, doi:10.1029/93GL01348.

Morrissey, T. N., K. W. Shallberg, A. J. Van Dierendonck, and M. J. Nicholson (2004), GPS receiver performance characterization under realistic ionospheric phase scintillation environments, *Radio Sci.*, *39*, RS1S20, doi:10.1029/2002RS002838.

Murad, E. (1984), The reaction of Sm^+ with O_2, *Int. J. Mass Spectrom. Ion Processes*, *58*, 159–164.

Murad, E., and D. L. Hildenbrand (1980), Dissociation energies of GdO, HoO, ErO, TmO, and LuO; correlation of results for the lanthanide monoxide series, *J. Chem. Phys.*, *73*, 4005–4011.

Reinisch, B. W., et al. (2009), New Digisonde for research and monitoring applications, *Radio Sci.*, *44*, RS0A24, doi:10.1029/2008RS004115.

Retterer, J. M. (2010), Forecasting low-latitude radio scintillation with 3-D ionospheric plume models: 1. Plume model, *J. Geophys. Res.*, *115*, A03306, doi:10.1029/2008JA013839.

Retterer, J., K. Groves, T. Pedersen, and R. Caton (2017), The electrodynamic effects of MOSC-like plasma clouds, *Radio Sci.*, *52*, doi:10.1002/2016RS006085.

Rosenberg, N. W., and G. T. Best (1971), Chemistry of barium released at high altitudes, *J. Phys. Chem.*, *75*(10), 1412–1418, doi:10.1021/j100680a009.

Stokes, C. S., and W. J. Murphy (1987), High altitude chemical release systems for project BIME (Brazilian ionospheric modification experiments) project IMS (ionospheric modification studies) project PIIE (polar ionospheric irregularities experiment) project Polar Arcs, *Air Force Geophys. Lab Final Rep. AFGL-TR-87-0231*, Gen. Sci., Inc.

Sultan, P. J. (1996), Linear theory and modeling of the Rayleigh-Taylor instability leading to the occurrence of equatorial spread *F*, *J. Geophys. Res.*, *101*, 26,875–26,891, doi:10.1029/96JA00682.

Towle, D. M. (1980), VHF and UHF radar observations of equatorial *F* region ionospheric irregularities and background densities, *Radio Sci.*, *15*, 71–86, doi:10.1029/RS015i001p00071.

Tsunoda, R. T. (1995), First incoherent-scatter measurements of the equatorial *E* layer obtained with the ALTAIR radar, *Geophys. Res. Lett.*, *22*, 847–850, doi:10.1029/95GL00299.

Tsunoda, R. T., M. J. Baron, and J. Owen (1979), Altair: An incoherent scatter radar for equatorial spread *F* studies, *Radio Sci.*, *14*, 1111–1119, doi:10.1029/RS014i006p01111.

Van Dierendonck, A. J., J. Klobuchar, and Q. Hua (1993), "Ionospheric Scintillation Monitoring Using Commercial Single Frequency C/A Code Receivers", in *Proceedings of the 6th International Technical Meeting of the Satellite Division of The Institute of Navigation (ION GPS 1993)*, pp. 1333–1342, Salt Lake City, Utah.

Williams, S., T. Beach, L. McNamara, and R. Daniell (2004), Metal Oxide Space Cloud Modeling and Simulation: SmOplus.for Release 1.0, Internal AFRL Report.

Yamamoto, M. (2008), Digital beacon receiver for ionospheric TEC measurement developed with GNU Radio, *Earth Planets Space*, *60*, e21–e24.

Zabusky, N. J., J. H. Doles III, and F. W. Perkins (1973), Deformation and striation of plasma clouds in the ionosphere: 2. Numerical simulation of a nonlinear two-dimensional model, *J. Geophys. Res.*, *78*, 711–724, doi:10.1029/JA078i004p00711.